A&A, 709, A190 (2026)
https://doi.org/10.1051/0004-6361/202658840

Astronomy & Astrophysics

Photoionisation cross-sections of HCN, HNC, and HNO

Ju Meng, Yitong Wang, and Kedong Wang*

School of Physics, Henan Normal University, Xinxiang 453007, PR China

Received 1 January 2026 / Accepted 13 April 2026

ABSTRACT

Aims. The primary aim of this work is to provide accurate photoionisation data for HCN, HNC, and HNO, including absolute total photoionisation cross sections and state-resolved partial cross sections. In addition, near-threshold structures in the photoionisation spectra are resolved with high precision.

Methods. In our calculations we employed a multichannel wavefunction constructed within the R-matrix framework, using configuration interaction to account for electronic correlation. The continuum is represented by a set of B-spline orbitals, enabling a highly accurate description of the scattering electron. This approach yields a more precise treatment of both the bound and continuum states compared with previous studies.

Results. We present total photoionisation cross sections from the ground states of HCN, HNC, and HNO, along with the partial cross sections that lead to various excited states of ions for photon energies from the ionisation thresholds up to 50 eV. A rich set of resonance features – absent in earlier calculations – is revealed near the ionisation thresholds for all three molecules. The resulting cross-section dataset is expected to be sufficiently accurate and comprehensive for most current modelling applications involving photon–molecule scattering for these systems.

Key words. ISM: molecules – photon-dominated region (PDR)

1. Introduction

Nitroxyl (HNO) together with hydrogen cyanide (HCN) and its isomer hydrogen isocyanide (HNC) constitute an important family of nitrogen-bearing molecules with diverse roles in astrophysical environments (Zamir et al. 2022). HCN is a major opacity source in carbon-rich stellar atmospheres and can substantially influence their thermal structure, and HNC has been robustly identified in evolved stars, such as WZ Cas, through infrared spectroscopic analyses (Harris et al. 2003). In contrast, HNO has not yet been securely detected in astrophysical observations. Nevertheless, owing to its high chemical reactivity and its proposed involvement in nitrogen–sulphur chemistry, HNO is expected to act as a short-lived but chemically significant intermediate in molecular evolution (Sebastian 2024; Miao et al. 2016).

Despite their close structural relationship, HCN, HNC, and HNO provide complementary diagnostic and chemical insights. The HCN/HNC abundance ratio is widely employed as a sensitive tracer of kinetic temperature in cold, dense regions of the interstellar medium (ISM) and in protoplanetary disks (Dawn et al. 2014; Hacar et al. 2022). In the ISM, HNC is observed to be nearly as abundant as its more stable isomer HCN (Zamir et al. 2022), and together with their ionic counterparts, these species participate in a complex chemical network that governs the evolution of dark molecular clouds. However, the observed HCN^+/HNC^+ abundance ratio remains difficult to reproduce in current astrochemical models, highlighting persistent uncertainties in the ionisation and destruction pathways of these molecules. Although HNO is observationally less constrained, chemical models predict strong coupling between HNO and other nitrogen- and sulphur-bearing species, implying a potentially important role in nitrogen cycling and molecular synthesis under similar physical conditions (Liu et al. 2007). Taken together, HCN, HNC, and HNO contribute to the nitrogen reservoir in disk chemistry and provide essential constraints for modelling molecular complexity and prebiotic pathways (Rimmer et al 2019; Rimmer et al. 2020).

Accurate photoionisation cross sections are a key ingredient in astrochemical and radiative-transfer models, as they directly determine molecular ionisation rates, charge balance, and subsequent reaction pathways in irradiated environments. For HCN and HNC, reliable photon–molecule interaction data are required to quantify the contribution of HNC to stellar atmospheric opacity and to model the extended HCN emission observed in low-density regions of the ISM (Paul et al. 2017). Partial photoionisation cross sections of HCN were calculated by Kreile et al. (1982) using a multiple-scattering model and by Wells et al. (1999) employing the single-channel Schwinger variational method. For HNC, Gans et al. (2019) measured the photoelectron spectrum for the $X^1\Sigma^+ \rightarrow X^2\Sigma^+$ transition at a fixed photon energy of 13 eV. Subsequently, Hrodmarsson et al. (2023) derived the photoionisation cross section based on these experimental results. To date, however, available experimental data remain largely confined to a narrow energy range, and theoretical studies are still sparse, with limited information available in the vicinity of the ionisation threshold.

For HNO, although its astrophysical detection has yet to be confirmed, theoretical studies of its reaction dynamics – most notably the benchmark reaction HNO + NO $\rightarrow$ N_2O + OH – provide key parameters for modelling nitrogen chemistry in star-forming regions and planetary atmospheres (Dianna et al. 1992; Sebastian 2024). The formation of N_2O, which has been detected in both interstellar and planetary environments, together with the production of OH, a fundamental interstellar radical, establishes a direct link between HNO-driven chemical pathways

* Corresponding author: wangkd@htu.edu.cn

and observable astrophysical species (Bergman et al. 2022). Consequently, even in the absence of direct detection, accurate photoionisation data for HNO can be used to constrain astrochemical models and assess its indirect impact on interstellar molecular evolution (Steven et al. 1997).

The primary aim of the present work is to provide an extensive and reliable dataset of photoionisation cross sections for HCN, HNC, and HNO, rather than to introduce a methodological advancement. All calculations were carried out using the open-source UKRmol+ package (Mašín et al. 2020), with electronic correlation treated at the configuration interaction (CI) level. A distinctive feature of this approach is the use of B-spline orbitals, which enable an accurate representation of the continuum states. The effectiveness of this strategy has been demonstrated in detail in our recent benchmark study on the photoionisation of OH radicals (Wang et al. 2021). This capability is particularly crucial for a reliable description of resonance structures and auto-ionisation processes near the ionisation threshold. These features, which were absent in previous studies, are identified here for the first time, notably in cases where they occur in close proximity to the ionisation thresholds. An energy grid step of 0.05 eV was employed throughout the calculations, which provides sufficient resolution to capture resonance structures within approximately 1 eV above the ionisation threshold.

2. Computational details

2.1. Theoretical method

The photoionisation cross sections in the length gauge are given by (Tennyson et al. 1986; Harvey et al. 2014)

$$\frac{d\sigma_{if}}{dk_f} = 4\pi^2 \alpha a_0^2 \omega |d_{if}(k_f) \cdot \hat{\epsilon}|^2, \tag{1}$$

where α is the fine structure constant, a_0 is the Bohr radius, ω is the photon energy in atomic units, and $\hat{\epsilon}$ is the polarisation vector of the ionising light in the molecular frame. $d_{if}(k_f)$ is the molecular frame transition dipole between the initial state, i, and a single continuum state, j, as a function of the ejected electron momentum, k_f.

If the molecular frame cannot be recovered, Eq. (1) must be orientationally averaged and in the case of a linearly polarised laser field one obtains

$$\overline{\left(\frac{d\sigma_{if}}{dk_f}\right)} = \frac{\sigma_{if}}{4\pi}[1 + \beta P_2(\cos\theta)], \tag{2}$$

where β is the asymmetry parameter, σ_{if} is the partial photoionisation cross section, P_2 is the second-order Legendre polynomial, and θ is the electron ejection angle between the photoelectron emission direction and photon polarisation direction in the case of linear polarisation. In the present paper, an R-matrix calculation is used to present the bound and the continuum wave functions in Eq. (1).

In an R-matrix approach (Burke et al. 2011), the configuration space of the scattering system is divided into two spatial regions: an inner region and an outer region. The inner region radius is chosen such that all short-range interactions are contained within it. The target wave function and corresponding charge density are assumed to be completely included in this sphere, and the electron-target interaction is represented through exchange and correlation potentials. In the outer region, long-range multipolar interactions of the scattering electrons with different target states are considered by using a single centre close-coupling (CC) approximation. At the interface, energy-independent solutions from the inner region are used to construct an energy-dependent R matrix.

In the inner region, both the continuum and the bound-state wave functions are given in terms of the basis functions, ψ_N^k, as

$$\Psi_f^{(-)N}(k_f) = \sum_k A_{fk}^{(-)}(k_f)\psi_k^N(x_1, \ldots, x_N), \tag{3}$$

$$\Phi_i^N = \sum_k B_{ik}\psi_k^N(x_1, \ldots, x_N), \tag{4}$$

where $A_{fk}^{(-)}(k_f)$ and B_{ik} are energy-dependent expansion coefficients determined from matching the wave functions Eqs. (3) and (4) to the well-known asymptotic solutions of the system, and x_i stands for the space-spin coordinates of the ith electron. The R-matrix basis functions ψ_k^N in turn are written in the CC form

$$\begin{aligned}\Psi_k^N(x_1, \ldots, x_N) = &\mathcal{A}\sum_{ij} a_{ijk}\phi_i^{N-1}(x_1, \ldots, x_{N-1})\,\eta_{ij}(x_N) \\ &+ \sum_p b_{kp}\chi_p^{(N)}(x_1, \ldots, x_N)\end{aligned} \tag{5}$$

Here, η_{ij} are the continuum orbitals orthogonalised with respect to the target orbitals, and $\mathcal{A}$ is the anti-symmetrisation operator. The coefficients a_{ijk} and b_{kp} are variational parameters determined through matrix diagonalisation. The summation in the second term of Eq. (5) runs over configurations χ_p, where all electrons are placed in target-occupied and virtual molecular orbitals (MOs). The choice of appropriate χ_p is crucial: these are L^2 configurations are required to properly account for polarisation effects as well as electron correlation arising from excitations within the neutral molecule.

To calculate the photoionisation of HCN, HNC, and HNO, we first constructed the MOs that ensure a good description of both continuum and bound wave functions. Then we constructed the target state wave functions with sufficient quality. Finally, we generated the continuum orbitals.

2.2. Target model

The equilibrium geometries of HCN, HNC, and HNO in their ground electronic states were optimised at the B3LYP/cc-pVQZ level of theory. Both HCN and HNC are linear structures. For HCN, the optimised C–H and C–N bond lengths are 1.092 and 1.207 Å, respectively. while for HNC the N–H and N–C bond lengths are 0.997 and 1.164 Å. The optimised geometry of HNO yields bond lengths of R(H–N) = 1.062 Å and R(N–O) = 1.197 Å, with a bond angle of ∠HNO = 108.8°. As both MOLPRO and UKRMOL+ only support Abelian point groups, the C_{2v} symmetry was adopted for HCN and HNC, and the C_s point group was used for HNO throughout all calculations. Target-state calculations were initiated by performing self-consistent-field Hartree–Fock (HF) calculations for the ground states of the HCN^+, HNC^+, and HNO^+ ions at the equilibrium geometries of the corresponding neutral molecules, using the selected basis set as implemented in the MOLPRO suite of programs (Werner et al. 2012). These calculations provided the initial sets of occupied and virtual MOs. To account for electron correlation effects beyond the self-consistent-field level, the target electronic states

Table 1. Vertical IPs (in eV) for HCN obtained with cc-pVDZ (BS1), cc-pVTZ (BS2), and cc-pVQZ (BS3) basis sets.

State	BS1	BS2	BS3	Expt
$X^2\Pi/(^2B_1,^2B_2)$	13.95	13.86	13.84	13.61[(a)]
				13.82[(b)]
$A^2\Sigma^+/^2A_1$	14.80	14.86	14.89	14.01[(a)]
				13.88[(b)]
$B^2\Sigma^+/^2A_1$	21.12	21.15	21.19	20.61[(b)]
$C^2\Pi/(^2B_1,^2B_2)$	21.20	21.18	21.21	

Notes. [(a)] From Kreile et al. (1982). [(b)] From Wells et al. (1999).

Table 2. Vertical IPs (in eV) for HNC obtained with cc-pVDZ (BS1), cc-pVTZ (BS2), and cc-pVQZ (BS3) basis sets.

State	BS1	BS2	BS3	Expt
$X^2\Sigma^+/^2A_1$	12.53	12.36	12.36	12.50[(a)]
$A^2\Pi/(^2B_1,^2B_2)$	15.56	15.40	15.40	
$B^2\Sigma^+/^2A_1$	21.50	21.27	21.29	
$C^2\Delta/(^2A_1,^2A_2)$	21.56	21.33	21.35	

Notes. [(a)] From Bieri et al. (1978).

Table 3. Vertical IPs (in eV) for HNO obtained with cc-pVDZ (BS1), cc-pVTZ (BS2), and cc-pVQZ (BS3) basis sets.

State	BS1	BS2	BS3	Expt
X^2A'	11.09	10.96	10.95	10.10[(a)]
A^2A''	13.40	13.29	13.30	
B^2A'	16.58	16.47	16.46	
C^2A''	17.28	17.11	17.07	

Notes. [(a)] From Lias et al. (1988).

were subsequently described using the complete active space (CAS) CI method.

The HF electronic configuration for the ground states of HCN^+ and HNC^+ ions are $1a_1^2$, $2a_1^2$, $3a_1^2$, $4a_1^2$, $5a_1^2$, $1b_1^2$ and $1b_2^1$ (Singh et al. 2022). Within the CAS–CI model, four electrons occupying the 1–$2a_1$ orbitals were frozen, while the remaining nine electrons were allowed to correlate freely within a set of nine active orbitals, namely 3–$7a_1$, 1–$2b_1$, and 1–$2b_2$, corresponding to a CAS(9,9) active space. For the HNO^+ ion, the HF ground-state electronic configuration is $1a'^2, 2a'^2, 3a'^2, 4a'^2, 5a'^2, 6a'^2, 7a'^2, 1a''^1$. In the target-state calculations, six electrons in the 1–$3a'$ orbitals were frozen, and nine electrons were treated as active in nine orbitals, namely 4–$10a'$, 1–$2a''$, again defining a CAS(9,9) active space.

Three correlation-consistent basis sets, cc-pVDZ, cc-pVTZ, and cc-pVQZ, were employed to assess the convergence and accuracy of the target-state wave functions. The calculated vertical ionisation potentials (IPs) of the first four low-lying ionic states are summarised in Tables 1, 2, and 3 for HCN, HNC, and HNO, respectively, together with available theoretical and experimental data for comparison. Overall, the three basis sets yield very similar IPs for all molecules considered, indicating satisfactory basis-set convergence. For HCN, the first IP associated with the $X^2\Pi$ state varies between 13.84 and 13.95 eV, in good agreement with the experimental value of 13.60 eV (Kreile et al. 1982) and the theoretical result of 13.82 eV reported by Wells et al. (1999). The second IP corresponding to the $A^2\Sigma^+$ state is predicted to be 0.80–0.88 eV higher than the experimental value of 14.10 eV (Wells et al. 1999) and approximately 1.0 eV higher than the CI result of 13.88 eV. For the third ionic state, the present IPs exceed the CI values of Wells et al. (1999) by about 0.6 eV. For HNC, the first IPs obtained with the three basis sets are tightly clustered in the range 12.36–12.53 eV, showing excellent agreement with the experimental value of 12.50 eV (Bieri et al. 1978), as reported in Table 2. This level of agreement further supports the reliability of the target-state description for the subsequent scattering calculations. In the case of HNO, the first IPs predicted by the three basis sets range from 10.95 to 11.09 eV and show minimal basis-set dependence. These values, however, exceed the experimental ionisation energy of 10.10 eV (Lias et al. 1988) by approximately 0.9 eV. This systematic overestimation likely reflects residual deficiencies in the treatment of polarisation and correlation effects. While an enlargement of the active space could potentially reduce this discrepancy, such an extension would substantially increase the computational cost and complexity of the subsequent electron–molecule scattering calculations.

Based on the convergence behaviour observed and considerations of computational feasibility, the cc-pVTZ basis set was selected as the optimal choice for all three molecular systems investigated in this work. Employing a consistent basis set across the HCN/HNC/HNO isomer series facilitates direct comparison of their electronic properties, while providing a balanced and reliable description of both valence and Rydberg states.

The primary effect of nuclear motion on photoionisation cross sections is the broadening and smoothing of resonance structures, particularly for shape and auto-ionising resonances, while the nonresonant background is generally less affected. Within the fixed-nuclei approximation, the neglect of vibrational motion can lead to artificially sharp and pronounced resonance features, especially in the near-threshold region. In contrast, experimental measurements inherently include vibrational averaging, which tends to wash out fine structures, reduce peak intensities, and slightly modify threshold behaviour. A more realistic description can be achieved by averaging over nuclear geometries (e.g., different bond lengths) or by performing a full vibrational averaging of the cross sections. In the present work, however, such calculations were not carried out in order to limit the computational cost and scope of the study. We note that the inclusion of vibrational motion is expected to smooth the resonance profiles but not to qualitatively alter the overall trends of the cross sections.

2.3. Inner and outer regions

In the inner region, continuum orbitals are traditionally constructed from Gaussian-type orbitals (GTOs) centred at the centre of mass of the molecular system. However, GTOs are not well suited to represent the highly oscillatory behaviour of true continuum wave functions, particularly over extended radial ranges and at higher collision or photon energies (Wang et al. 2021). As a result, the size of the R-matrix sphere and the range of collision energies that can be treated using GTO-based continua are inherently limited. A more suitable basis for this purpose is provided by B-spline functions. B-spline basis sets enable an accurate description of continuum electrons with higher kinetic energies and allow for significantly enlarged inner

regions, making it possible to treat larger molecular targets as well as systems with more diffuse electronic states. Accordingly, B-spline-type orbitals (BTOs) were employed in the present work to represent the continuum. The BTO continuum orbitals were orthogonalised to the target MOs, and those with an overlap of less than 10^{-5} were discarded, following the procedure described in Morgan et al. (1997). The order of the B-splines and the maximum number of radial B-splines were chosen as $k = 6$ and $N = 15$, respectively. The first two radial B-splines were excluded from the basis set, as they possess non-zero first derivatives at the origin.

In the present calculations, the L^2 configurations appearing in Eq. (5) are classified into two types: $(\text{core})^n(\text{CAS})^{m-n-1}(\text{virtual})^1$ and $(\text{core})^n(\text{CAS})^{m-n}$, where n denotes the number of frozen electrons and m is the total number of electrons in the neutral molecule. The inclusion of a sufficiently large number of target states is essential for achieving convergence of the CC expansion and for avoiding unphysical pseudo-resonances that may otherwise appear at higher collision energies due to the omission of relevant target states. In this work, a total of 60 target states were included in the CC expansion, which was found to be sufficient to ensure convergence of the scattering calculations. In the present approach, the MOs of the molecular ion are employed to describe the ground-state wave function of the corresponding neutral molecule. Although this constitutes an approximate treatment of the neutral ground state, it significantly simplifies the evaluation of transition dipole moments, as the same set of MOs is used consistently for both the initial and final electronic states. The R-matrix radius was set to 15 a_0, and the scattering wave functions were propagated outwards to 100 a_0 to ensure proper asymptotic behaviour.

3. Tests of models

3.1. HCN

The total photoionisation cross sections from the ground state of HCN, calculated using a CAS(10,9) description for the inner region, are presented in Fig. 1. To assess the convergence of the calculated cross sections, three models with different R-matrix radii and maximum continuum angular momentum values, l_{max}, were examined. As shown in Fig. 1a, for an R-matrix radius of 13 a_0, the cross sections obtained with $l_{max} = 6$ are almost indistinguishable from those calculated with $l_{max} = 4$, indicating that $l_{max} = 6$ is sufficient to achieve convergence of the photoionisation cross sections for HCN. Furthermore, when $l_{max} = 6$ is employed, the cross sections computed with R-matrix radii of 13 a_0 and 15 a_0 are very similar, demonstrating that an R-matrix radius of 15 a_0 provides a converged description of the inner-region dynamics.

The parameters controlling the evaluation of the single-electron nuclear-attraction and two-electron Coulomb integrals determine the highest partial wave retained in the Legendre expansion of the Coulomb interaction when computing the BTO integrals. In this work, we systematically examined the sensitivity of the calculated results to different truncation limits in these Legendre expansions. Figure 1b shows convergence tests for HCN performed using three different maximum angular-momentum cutoffs in the Legendre expansions of the mixed nuclear-attraction and two-electron integrals. On the basis of these tests, maximum Legendre orders of 35 and 25 were adopted for the one-electron and two-electron integrals, respectively, and these values were used consistently in all subsequent calculations.

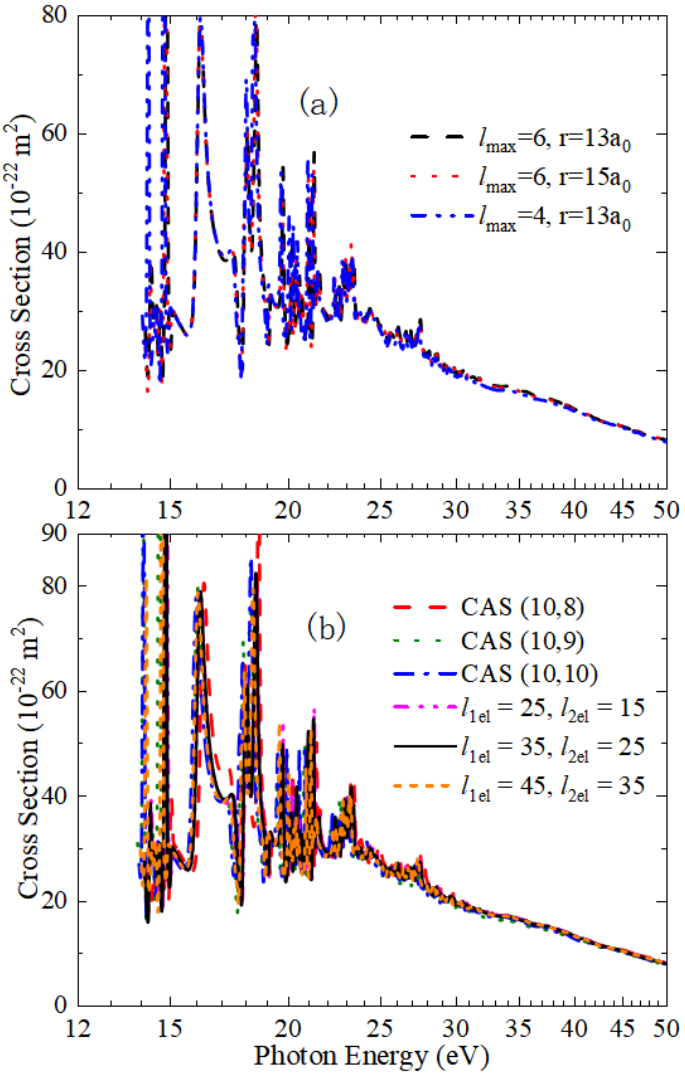

Fig. 1. Photoionisation cross sections for HCN determined using different models.

To assess the convergence of correlation and polarisation effects, three different active spaces were examined. In each case, nine active electrons were distributed among three configurations – CAS(10,8), CAS(10,9), and CAS(10,10). The resulting total photoionisation cross sections obtained with the three active-space models are displayed in Fig. 1b. The cross sections exhibit nearly identical amplitudes across all three cases, indicating that the calculated results converge well with respect to the treatment of correlation and polarisation effects. Based on these systematic convergence tests, and taking into account the available computational resources, an optimised theoretical protocol was established for the calculation of photoionisation cross sections of HCN. The final computational model employs the cc-pVTZ basis set, a CAS(10,9) active space, a maximum continuum angular momentum of $l_{max} = 6$ in the CC expansion, and an R-matrix radius of 15 a_0. The photoionisation results obtained using this model are discussed in detail in the following section. In addition, these test calculations indicate that the uncertainty in the calculated cross sections is less than 20%.

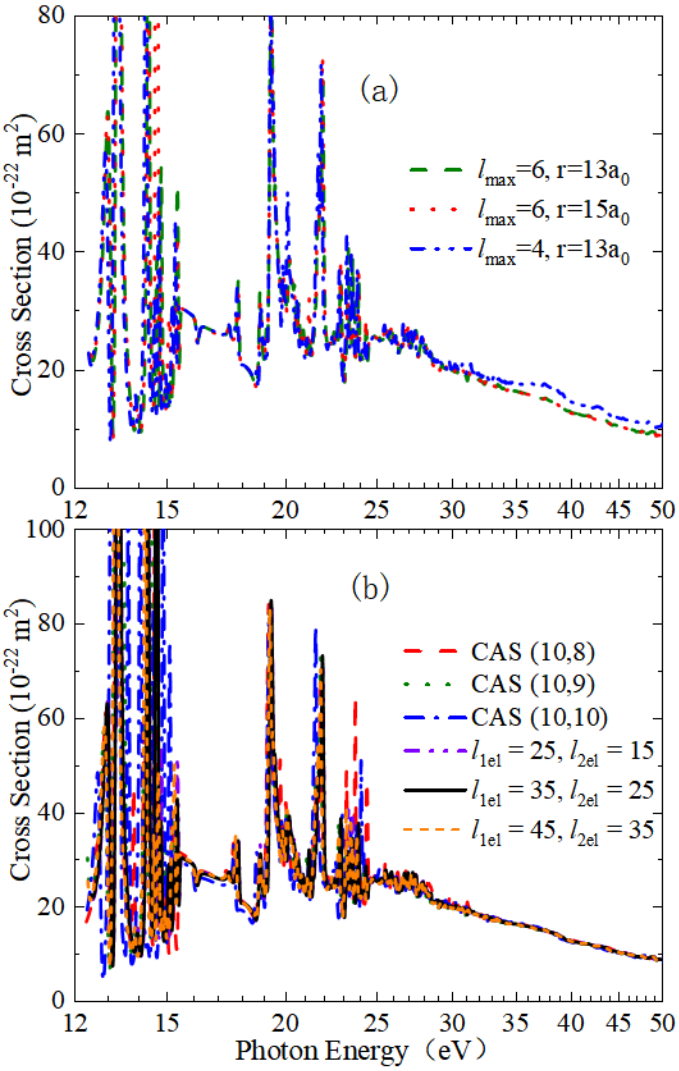

Fig. 2. Photoionisation cross sections for HNC determined using different models.

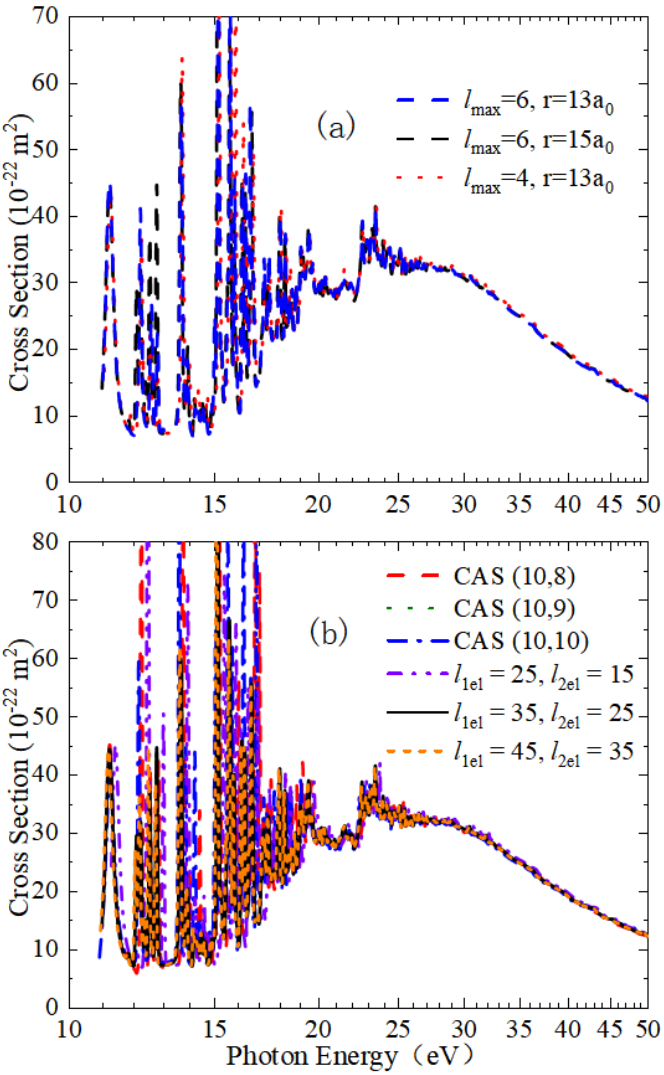

Fig. 3. Photoionisation cross sections for HNO determined using different models.

3.2. HNC

The total photoionisation cross sections from the ground state of HNC with different models using the CAS(10,9) active space for HNC^+ target are presented in Figure 2a. The cross section results with l_{max} = 4 are slightly higher than that of l_{max} = 6 in the energy region above 30 eV with an R-matrix radius of r = 13 a_0, indicating that l_{max} = 4 may be not enough to obtain the convergence of the cross section for HNC. Furthermore, cross sections calculated with R-matrix radii of both 13 a_0 and 15 a_0 using l_{max} = 6 show remarkable consistency, thereby validating the convergence of the 15 a_0 radius selection.

Figure 2b presents convergence tests for HNC employing three distinct maximum angular momentum values in the expansions of mixed nuclear attraction (l_{1el}) and two-electron (l_{2el}) integrals. As shown in the figure, all three combinations yield nearly identical cross-section magnitudes, indicating that the (25,15) combination is already converged. Considering the overall computational cost, we adopted the (35,25) combination for the one-electron and two-electron integrals, which were subsequently adopted in the following computations.

Three distinct active space configurations – CAS(10,8), CAS(10,9), and CAS(10,10) – are used to test the convergence of the polarisation effects. The resulting photoionisation cross sections based on these three active spaces are also displayed in Figure 2b, demonstrating consistent cross-section amplitudes across all models, confirming the convergence of our computational approach. The final computational framework employs the cc-pVTZ basis set, a CAS(10,9) active space, and l_{max} = 6 in the CC expansion. The physical implications and spectroscopic insights derived from this optimised model will be comprehensively discussed in the subsequent section. The uncertainty in the calculated cross sections is less than 20%, as shown in Figure 2.

3.3. HNO

The total photoionisation cross sections of ground-state HNO, calculated with the CAS(10,9) active space, are shown in Figure 3a. Numerical convergence was assessed by systematically varying the R-matrix radius and the maximum partial wave. For an R-matrix radius of 13 a_0, the cross sections obtained with l_{max} = 4 and l_{max} = 6 are nearly identical, indicating that l_{max} = 6 ensures angular momentum convergence. In addition, results calculated with radii of 13 a_0 and 15 a_0 at l_{max} = 6 are essentially indistinguishable, confirming the adequacy of the 15 a_0 R-matrix radius.

Figure 3b shows the convergence of the HNO calculations with respect to the maximum angular momentum used in the nuclear attraction and two-electron integral expansions. These tests justify the adoption of Legendre expansion orders of 35 and 25 for the one-electron and two-electron terms, respectively, which are used throughout this work. Three active spaces – CAS(10,8), CAS(10,9), and CAS(10,10) – were also examined. Despite the strong dependence of the Hilbert space size on the choice of active orbitals, the photoionisation cross sections shown in Figure 3b display very similar spectral amplitudes for all models, demonstrating the robustness of our approach. Based on these convergence tests, the final calculations employ a CAS(10,9) active space, partial waves up to $l_{max} = 6$, and an inner-region radius of 15 a_0. The uncertainty in the resulting cross sections is estimated to be less than 20%. The physical and spectroscopic implications of this optimised setup are discussed below.

4. Results and discussions

4.1. HCN

The total and partial photoionisation cross sections from the $X^1\Sigma^+$ ground state of HCN in the energy range 12.86–50 eV are presented in Figure 4. Below 14.86 eV, the total cross sections obtained with the CC model exhibit numerous sharp peaks, which can be attributed to a Rydberg series converging to the $X^2\Pi$ state of the HCN^+ ion. In the energy region from 14.86 to 21.20 eV, the observed peaks correspond to two Rydberg series converging to the $A^2\Sigma^+$ and $B^2\Sigma^+$ ionic states of HCN^+. The partial cross sections for the $X^2\Pi$ channel calculated using the static-exchange (SE) model, together with available results, are also shown in Figure 4a. For ease of comparison, the existing cross sections have been shifted so that their threshold aligns with that of the CC model. As illustrated in the figure, the SE model predicts a broad shape resonance centred at 18.7 eV. In the CC model, this resonance is expected to shift to lower energy. However, the presence of several overlapping auto-ionising states precludes a clear identification of its exact position. In comparison with the CC results, the SE model significantly underestimates the magnitude of the cross sections. This discrepancy arises from the frozen-core approximation inherent in the SE model, which neglects both electron correlation and channel-coupling effects. Wells et al. (1999) performed single-channel scattering calculations for HCN photoionisation using the Schwinger variational method. The cross sections for the $X^2\Pi$ channel obtained from our CC model exhibit numerous resonance peaks that are not clearly resolved in the calculations by Wells et al., particularly in the energy region below 28 eV. Overall, our cross sections are approximately 2–3 $\times 10^{-22}$ m^2 larger. In the single-channel Schwinger variational approach, polarisation effects are incorporated implicitly through the inclusion of correlation functions in the trial wave function, which account for short-range electron correlation and target distortion. However, genuine interchannel coupling is absent. In contrast, the multichannel R-matrix method describes polarisation effects through explicit coupling between the ground and excited ionic states, allowing for a systematic representation of both short- and long-range polarisation. Moreover, interchannel coupling is treated explicitly, enabling an accurate description of resonance structures, auto-ionisation processes, and state-resolved photoionisation cross sections.

The partial photoionisation cross sections for ionisation leading to the $A^2\Sigma^+$ and $B^2\Sigma^+$ states of HCN^+ obtained with the CC model are shown in Figure 4b, together with the available results of Wells et al. (1999) and Kreile et al. (1982). For ionisation into the $A^2\Sigma^+$ state, our cross sections are systematically larger than those of Wells et al. by approximately 2–5 $\times 10^{-22}$ m^2 over the entire energy range considered. As discussed above, these differences can be attributed to the inclusion of multichannel coupling in the CC model. In contrast, for ionisation into the $B^2\Sigma^+$ state, our results are in very good agreement with the Schwinger variational calculations. Kreile et al. (1982) computed partial photoionisation cross sections using a multiple-scattering model. For the $X^2\Pi$ and $A^2\Sigma^+$ channels of HCN^+, our calculated cross sections are consistently higher than theirs, whereas for the $B^2\Sigma^+$ channel our values are lower. Given the semi-empirical nature of their approach, these discrepancies mainly reflect the more accurate description of polarisation and electron-correlation effects in the present calculations. Wells et al. (1999) also noted that several narrow resonant features in the results of Kreile et al. (1982) originate from inherent limitations of the multiple-scattering method. For this reason, these resonances are not discussed here.

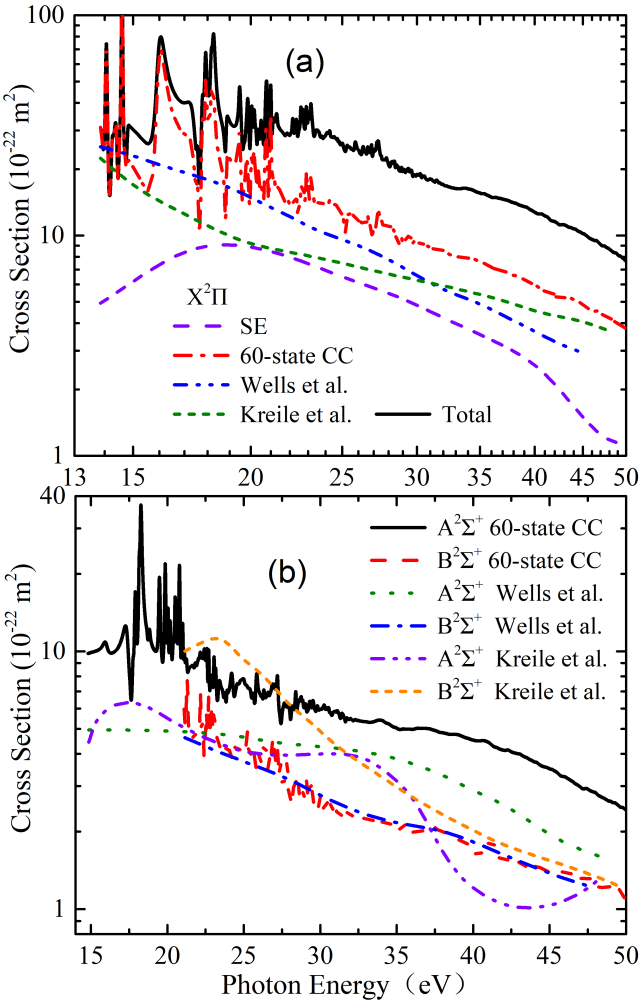

Fig. 4. Total and partial cross sections from the photoionisation of the HCN ground state.

4.2. HNC

The total photoionisation cross section of HNC from its $X^1\Sigma^+$ ground state, calculated using the CC model, is presented in

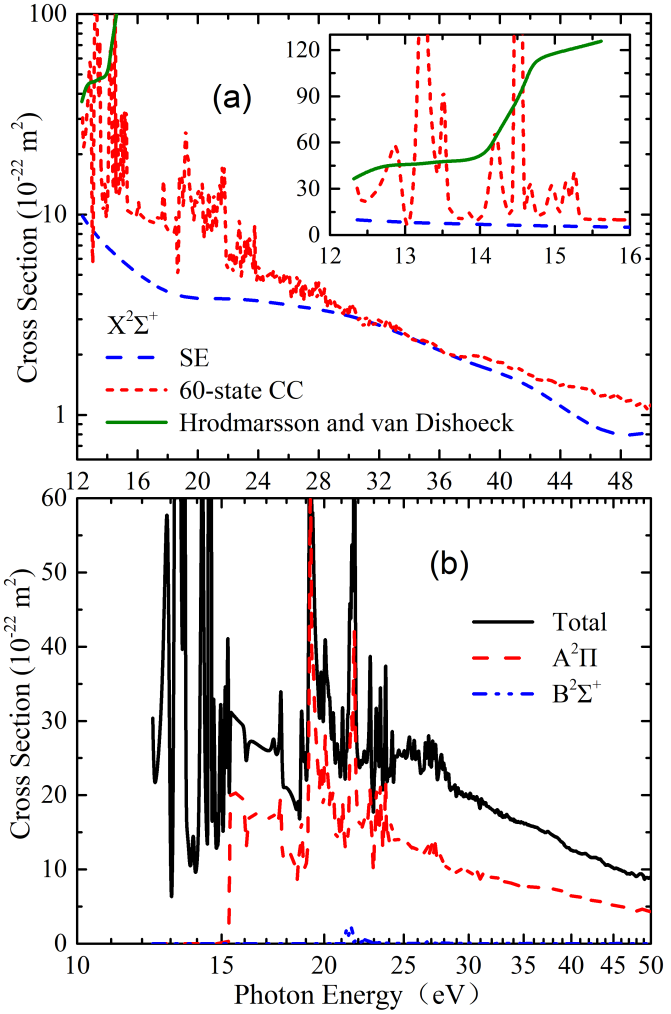

Fig. 5. Total and partial cross sections from the photoionisation of the HNC ground state.

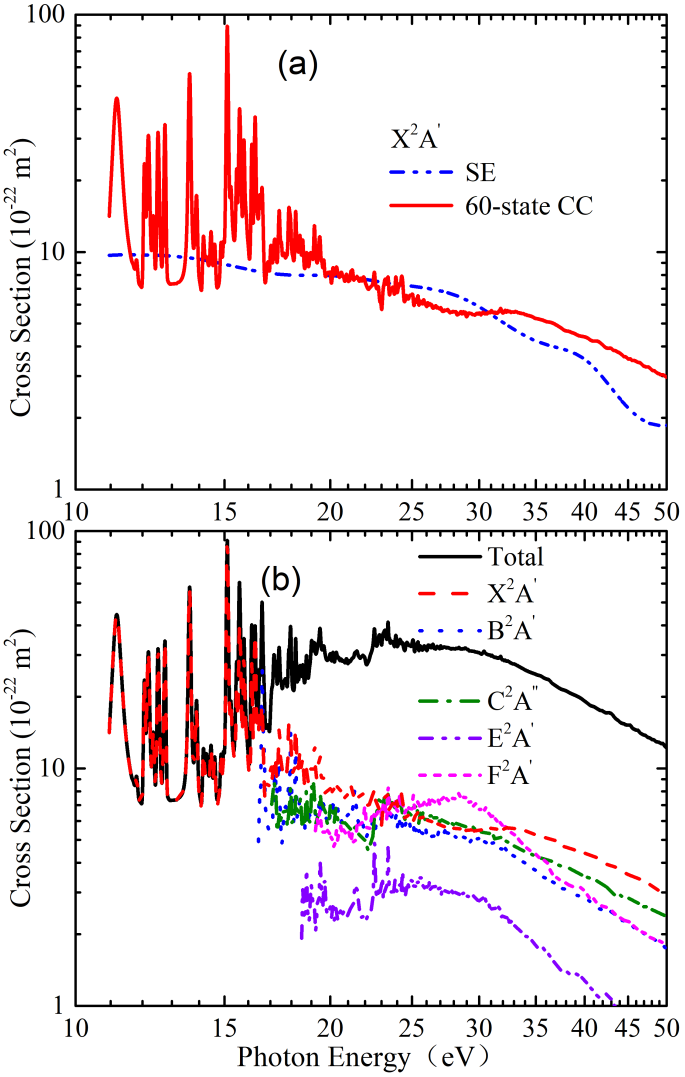

Fig. 6. Total and partial cross sections from the photoionisation of the HNO ground state.

Figure 5. Compared with its isomer HCN, HNC exhibits a very similar overall cross-section magnitude. Below 15.4 eV, distinct auto-ionisation features are observed and can be assigned to a Rydberg series converging to the $A^2\Pi$ state of the HNC^+ ion, which lies 3.04 eV above the cationic ground state.

The partial photoionisation cross sections leading to the $X^2\Sigma^+$, $A^2\Pi$, and $B^2\Sigma^+$ states of HNC^+ are also shown in Figure 5. Experimentally, HNC has been efficiently produced in the gas phase using a flow-tube reactor with a suitable precursor ($HN{=}CH_2$), and its photoionisation from the $X^1\Sigma^+$ state of HNC to the $X^2\Sigma^+$ state of HNC^+ was measured by Gans et al. (2019). Based on these measurements, Hrodmarsson et al. (2023) derived the threshold photoelectron spectrum and the corresponding absolute photoionisation cross sections. As shown in Figure 5, their results are higher than our CC values above 14.7 eV. However, the available experimental data cover only a very narrow energy range. Moreover, the presence of sharp auto-ionisation resonances in our calculations within this region makes a direct comparison with the experimentally extrapolated results – which include vibrational contributions – difficult. For the $X^2\Sigma^+$ channel, we also performed calculations using the SE model. As illustrated in Figure 5a, the SE cross sections are slightly lower than the CC results below 30 eV and above 38 eV, reflecting the role of electron-correlation effects included in the CC model. It is noteworthy that the cross section for the $A^2\Pi$ state is approximately twice that of the $X^2\Sigma^+$ state and therefore provides the dominant contribution to the total cross section. In contrast, the $B^2\Sigma^+$ cross section is very small and contributes negligibly to the total cross section.

4.3. HNO

The total and partial photoionisation cross sections of HNO from its ground state, calculated using the CC model, are presented in Figure 6. The dominant partial cross sections correspond to five ionic states of HNO^+: X^2A', B^2A', C^2A'', E^2A', and F^2A'. The spectra start at 10.96 eV, corresponding to the first vertical IP. The oscillatory structure observed in the X^2A' channel immediately above threshold originates from ionisation of the $1a''$ electron. To assess the role of electron correlation, additional calculations were performed using the SE model, as shown in Figure 6a. Overall, the SE and CC results are in good agreement, indicating that correlation effects are relatively minor for the X^2A' channel.

Above 30 eV, the cross sections for the X^2A', B^2A', C^2A'', and F^2A' states become relatively smooth and exhibit comparable magnitudes, all gradually decreasing over the 30–50 eV

range. In the low-energy region, numerous narrow auto-ionising resonances are observed, which are characteristic of the fixed-nuclei approximation. In contrast, the high-energy region is dominated by broader resonance features. In particular, a pronounced broad resonance appears around 28 eV in the F^2A' channel, while another is found near 34 eV in the X^2A' cross section. These broad resonances may provide favourable targets for future experimental investigations of HNO photoionisation. The cross section associated with the E^2A' state is consistently smaller – by approximately 2–4 $\times$ 10^{-22} m^2 – than those of the other channels across the entire energy range, reflecting its comparatively weaker transition strength.

5. Summary

We have carried out a comprehensive investigation of the photoionisation of HCN, HNC, and HNO, presenting both total and state-resolved partial cross sections. The calculations were performed using the multichannel R-matrix method, with a B-spline basis employed to represent continuum orbitals and electronic correlation treated at the CI level. This approach provides a more accurate and balanced description of both bound and continuum states than those adopted in earlier studies.

A systematic assessment of key computational parameters was conducted for all three systems, including the R-matrix radius, the number of partial waves, the choice of active space, and the maximum angular momentum used in the Legendre expansions of the mixed nuclear-attraction and two-electron integrals. Through extensive convergence tests, optimised computational models were established, achieving a careful balance between numerical accuracy and computational cost. These test calculations indicate that the uncertainties in the cross sections for all three molecules are below 20%.

Using these optimised models, we obtained reliable photoionisation cross sections from the ground states of HCN, HNC, and HNO. The resulting data provide absolute cross sections together with well-resolved resonance structures and positions. Where available, detailed comparisons with previous studies were performed. The present results therefore offer valuable benchmarks for assessing electron-correlation treatments in molecular photoionisation and are expected to support spectroscopic studies in interstellar and planetary environments.

In astrochemical models, photoionisation cross sections directly determine molecular ionisation rates, which are key parameters governing the chemical evolution of interstellar media and protoplanetary disks. These rates are obtained by integrating the product of the photon flux and the energy-dependent cross section over the relevant radiation field. Consequently, the magnitude and energy dependence of the cross sections control the efficiency of molecular ionisation under astrophysical radiation fields, such as stellar UV and cosmic-ray–induced photons. In particular, resonance structures near the ionisation threshold can significantly enhance ionisation rates in low-energy radiation environments, thereby influencing ion–molecule reaction networks, electron production, and the overall ionisation balance. Accurate cross-section data are therefore essential for reliable predictions of molecular abundances and chemical pathways in such environments.

Given the current scarcity of photoionisation data for these species, we anticipate that the present work will stimulate further experimental and theoretical studies. Such data are important for a wide range of applications, including aeronomy, astrochemistry, and plasma modelling.

Data availability

The data presented in this article are available at Zenodo: https://doi.org/10.5281/zenodo.19564068

Acknowledgements. This work was supported by the Natural Science Foundation of Henan Province under Grant No. 252300421490 and the Natural Science Foundation of China under Grant No. 12304270.

References

Bergman, P., Lerner, M. S., Olofsson, A. O. H., et al. 2022, A&A, 660, A118
Bieri, G., & Jonsson, B. O. 1978, Chem. Phys. Lett., 56, 446
Burke, P. G. 2011, R-Matrix Theory of Atomic Collisions (Berlin, Heidelberg: Springer-Verlag)
Dawn, M. G., Eric, H., Graninger D. M., et al. 2014, ApJ, 787, 74
Dianna, L., & Paul, M. 1992, J. Phys. Chem., 96, 2471
Gans, B., Garcia, G. A., Boyé-Péronne, S., et al. 2019, Phys. Chem. Chem. Phys., 21, 2337
Hacar, A., Bosman, A. D., & Van Dishoeck, E. F. 2020, A&A, 635, A4
Harris, G. J., Pavlenko, Y., Jones, H. R. A., & Tennyson, J. 2003, MNRAS, 344, 1107
Harvey, A. G., Brambila, D. S., Morales, F., & Smirnova, O. 2014, J. Phys. B., 47, 215005
Hrodmarsson, H. R., & van Dishoeck, E. F. 2023, A&A, 675, A25
Kreile, J., Schweig, A., & Thiel, W. 1982, Chem. Phys. Lett. 87, 473
Lias, S. G., Bartmess, J. E., Liebman, J. F., et al. 1988, J. Phys. Chem. Ref. Data, Suppl., 17, 1
Liu, Y., Liu, W., Li, H., Yang, Y., & Cheng, S. 2007, Int. J. Quantum Chem., 107, 396
Mašín, Z., Benda, J., Gorfinkiel, J. D., Harvey, A. G., & Tennyson, J. 2020, Comput. Phys. Commun., 249, 107092
Miao, Z. R., & King, S. B. 2016, Nitric Oxide, 57, 1
Morgan, L. A., Gillan, C. J., Tennyson, J., & Chen, X. 1997, J. Phys. B., 30, 4087
Paul, F. G., & Jens, K. 2017, ApJ, 841, 25
Rimmer, P. B., & Rugheimer, S. 2019, Icarus, 329, 124
Rimmer, P. B., Ferus, M., Waldmann, I. P., et al. 2020, ApJ, 888, 21
Sebastian, A. S. 2024, Redox Biochem. Chem., 8, 100024
Singh, J., & Tennyson, J. 2022, Eur. Phys. J. D, 76, 242
Steven, W. B., Betsy, M. R., & Chabalowski, C. F. 1997, J. Phys. Chem. A, 101, 9430
Tennyson, J., Noble, C. J., & Burke, P. G. 1986, Int. J. Quantum Chem., 29, 1033
Wang, K. D., Liu, J., Zhang, H. X., & Liu, Y. F. 2021, Phys. Rev. A, 103, 063101
Wells, M., & Lucchese, R. R. 1999, Phys. Rev. A, 60, 4519
Werner, H. J., Knowles, P. J., Knizia, G., Manby, F. R., & Schütz, M. 2012, WIREs Comput. Mol. Sci., 2, 242
Zamir, A., & Stein, T. 2022, J. Chem. Phys., 156, 054307